Accuracy of Shack–Hartmann wavefront sensor using a coherent wound fibre image bundle

Jessica R. Zheng[1], Michael Goodwin and Jon Lawrence

Australian Astronomical Observatory, 105 Delhi Road, North Ryde, NSW 2113, Australia
[1]Email: jessica.zheng@aao.gov.au

Abstract

Shack–Hartmannwavefront sensors using wound fibre image bundles are desired for multi-object adaptive optical systems to provide large multiplex positioned by Starbugs. The use of a large-sized wound fibre image bundle provides the flexibility to use more sub-apertures wavefront sensor for ELTs. These compact wavefront sensors take advantage of large focal surfaces such as the Giant Magellan Telescope. The focus of this paper is to study the wound fibre image bundle structure defects effect on the centroid measurement accuracy of a Shack–Hartmann wavefront sensor. We use the first moment centroid method to estimate the centroid of a focused Gaussian beam sampled by a simulated bundle. Spot estimation accuracy with wound fibre image bundle and its structure impact on wavefront measurement accuracy statistics are addressed. Our results show that when the measurement signal-to-noise ratio is high, the centroid measurement accuracy is dominated by the wound fibre image bundle structure, e.g. tile angle and gap spacing. For the measurement with low signal-to-noise ratio, its accuracy is influenced by the read noise of the detector instead of the wound fibre image bundle structure defects. We demonstrate this both with simulation and experimentally. We provide a statistical model of the centroid and wavefront error of a wound fibre image bundle found through experiment.

Keywords: instrumentation: adaptive optics

1 INTRODUCTION

Shack−Hartmann wavefront sensor (SHWFS) is a widely applied technique for measuring wavefront aberrations for adaptive optics (AO) (Hardy 1998). A fibre image bundle-based SHWFS could enable a more robust and flexible wavefront measurement for extremely large telescope that are currently being built or proposed. In particular, Multi-object adaptive optics (MOAO) systems can maximise the scientific output of those large aperture wide-field telescopes, like the Giant Magellan Telescope (GMT). For MOAO to be realised on telescopes, many wavefront sensors are needed to be deployed across the focal plane, localising at each science target. We proposed two types of wavefront sensor by using fibre image bundles (Goodwin et al. 2014; Zheng et al. 2014) where the image formed on the wavefront sensor can be relayed by a fibre image bundle to a more convenient location. The concept of an image bundle-based SHWFS for Starbugs has been detailed by Goodwin et al. (2014) with an early lab prototype built for the GMT (Goodwin et al. 2015). The advantage of these miniature wavefront sensors is that each device can be fit in one 'Starbug' fibre positioning device currently under development at Australian Astronomical Observatory (Gilbert et al. 2012, Staszak et al. 2016). Multiple

miniature wavefront sensors can be multiplexed to a common low noise camera and deployed in multiple locations according to the available natural or laser guide stars on the telescope focal plane and position reconfigured to meet different observations. It can potentially be used for ground-layer AO in which a single deformable mirror for ground atmospheric disturbance correction can be controlled by averaging the signals from multiple wavefront sensors pointing in widely separated directions (Ammons et al. 2010; Ono et al. 2016). Another application for image bundle-based SHWFS is active optics, where a large number of wavefront sensors can help with the mirror alignment under slow changing conditions.

In our previous two publications, the fibre image bundle discussed is the polymer coherent fibre image bundle. Its performance (Richards et al. 2017) is comparable to the conventional wavefront sensor, however one major shortcoming is its rigidity and transmission loss, particularly in the near infra-red. For large telescope wavefront sensing, the relaying image fibre bundle needs to be more than a few millimetres in diameter to allow for size of the needed microlens array (e.g. 50×50 apertures to accommodate more sub-apertures within the telescope pupil to be able to measure the wavefront more precisely). A polymer fibre image bundle of this
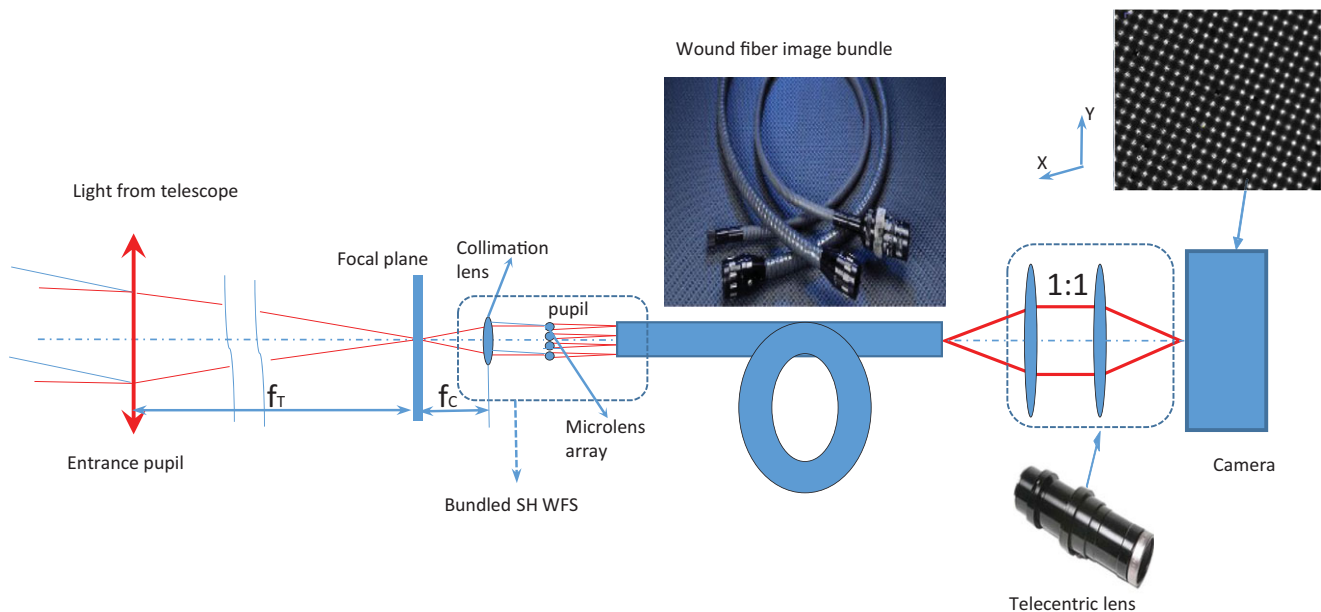
Figure 1. Shack–Hartmann wavefront sensor with coherent fibre image bundle.

size will not be able to move around freely due to bundle rigidity. Other than the polymer fibre image bundle, there are some other flexible image fibre bundles currently available on the market (SCHOTT 2007) such as the Schott leached fibre image bundle and the wound fibre image bundle. The leached fibre image bundles have a maximum diameter of about 1.5 mm and therefore are not suitable for large aperture wavefront sensing. However, the wound fibre image bundle can easily be scaled up to tens of millimetres and hence the best candidate for a Starbug WFS.

The measurement sensitivity of a conventional SHWFS mainly depends on the detector sampling, photon noise from the guide star, read-out noise of the camera, the speckle noise introduced by the atmosphere and algorithm to find the centroids (Irwan & Lane 1999; Thomas et al. 2006). A detailed examination of the different centroiding methods and image-processing techniques can be found in Nightingale & Gordeyev (2013).

While the wound fibre image bundle with high core density can relay the image effectively, its application in the SHWFS has to be examined carefully because of its unique properties. In this paper, we focus on the simulation of the Schott 'demo' wound fibre image bundle defects impact on the centroiding measurement accuracy. We report on the experimental measurements of this demo wound fibre image bundle using our test bench, configured as a SHWFS.

2 CONCEPT OF THE SHACK–HARTMANN WAVEFRONT SENSOR WITH WOUND FIBRE IMAGE BUNDLE

Figure 1 shows the details of SHWFS with the wound fibre image bundle. Note that the SHWFS we discuss here actually

includes a collimating lens in front of a microlens array. The light from a telescope pupil is collimated through the collimating lens and the telescope pupil is re-sized and re-imaged onto the microlens array. The incoming light forms a diffraction limited spot array on the focal plane of the microlens array where the wound fibre image bundle is placed. The spot array image is then relayed by the fibre image bundle. At the far end, the bundle surface (spot array) is then re-imaged onto the camera. By measuring the centroid of each spot in the spot array, the slope of the inbound wavefront can be found and hence the wavefront reconstructed. Since the collimating lens is of small size and good optical quality, the whole bundled SHWFS can be fit into the Starbug which is going to be located at the telescope focal plane.

3 PROPERTIES OF THE WOUND FIBRE IMAGE BUNDLE

The wound fibre image bundles normally comprise tens of thousands optical fibres of either glass or polymer cores. Ideally, each fibre is considered to act as an independent waveguide. The wound fibre image bundle can be made with sizes up to tens of millimetres depending on the manufacturing. Because individual fibre positions at both ends of the bundle match, an image projected onto the input face is transmitted unaltered to the output end. This is demonstrated by Figure 2(a) where a Thorlabs target is illuminated and imaged, with a magnification of 1 onto the input face of the wound fibre image bundle and at the output end, it is then re-imaged with a magnification of 2 onto the detector.

The wound fibre image bundle used in our discussion is from Schott North America as a demonstration unit. It is 4 mm by 4 mm in square shape and 1m in length. Its
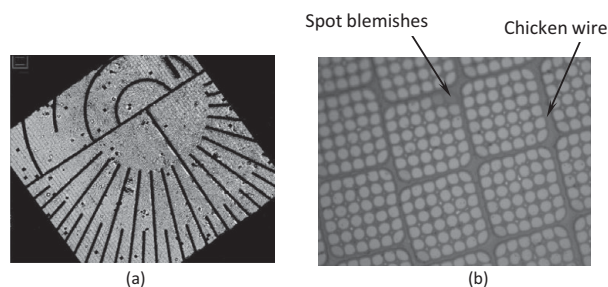
Figure 2. (a) Image of a target. (b) End image of the wound fibre image bundle with 40X magnification.
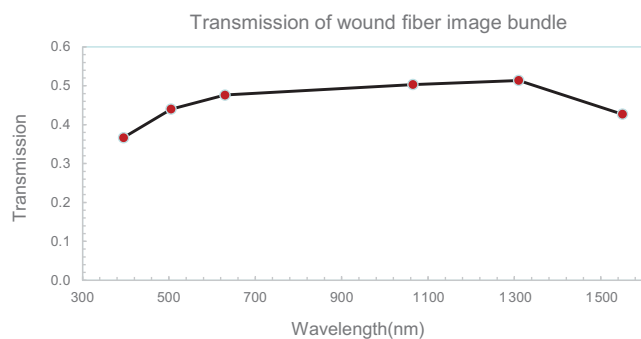

Figure 3. Measured transmission of wound fibre image fibre bundle.

numerical aperture is 0.6. The individual fibre size is 10 μm with core size of 8 μm. It is typically fabricated by winding a tile of 6×6 multi-fibre bundle cell into a single-layer ribbon on a cylindrical mandrel, assembling layers in a separate laminating operation, then cutting through and polishing the ends (SCHOTT 2007). Its end surface is shown in Figure 2(b).

3.1. Optical transmission

To verify the operation of this demo wound fibre image bundle, its optical transmission was first measured. Figure 3 shows its transmission for the wavelength range from 390 to 1 550 nm with input beam *F*-number of 8. Note that it includes the surface Fresnel reflection from both the ends. Its transmission is above 40% for most visible and near infrared range. This implies that the demo wound fibre image bundle could be used for wavefront sensing in the near infra-red. The loss mostly comes from the fill factor of the fibre image bundle which is the inherent property of image bundles.

3.2. Defects

The main two defects of the wound fibre image bundle are blemishes and distortion(SCHOTT 2007). The blemishes including spot and line blemishes (also known as 'Chicken Wire') are shown in Figure 2(b). The spot blemishes are the small areas (or groups of fibres) with reduced or no trans-
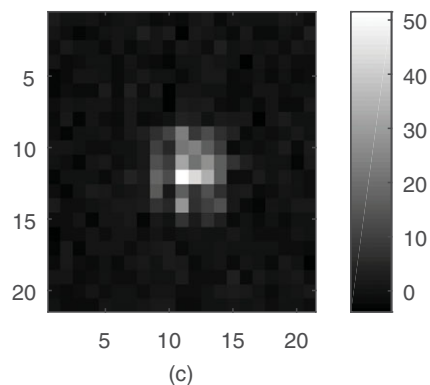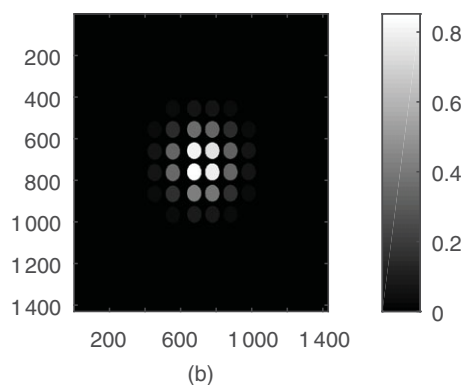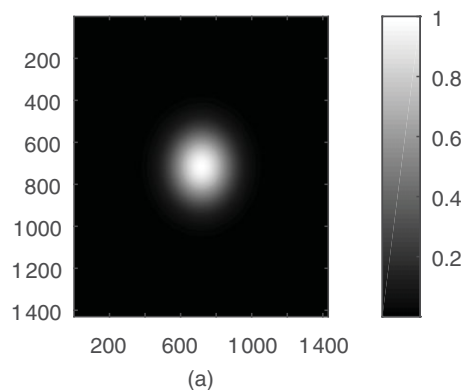

Figure 4. Simulated focused spot with equivalent Airy size of 66.8 μm on a 1 430 × 1 430 grid. (a) Pure Gaussian Beam. (b) Sampled by fibre image bundle. (c) Sampled by sCMOS chip (SNR:17).

mission. The line blemishes are defined as a pattern of dark fibres that are two to four fibres wide at the fibre tile boundary. They are caused by damage to the fibres at the outside edges of the cell fibre array which can be caused by contamination, or improper temperature and pressure control in the pressing operation. Line blemishes are quantified by its length and quantity. The distortion could manifest itself in two forms: shear and gross distortion where the first one is defined as a lateral displacement that causes a straight line to be imaged as a 'break' line. It is caused by the misalignment of fibre tiles along the length. This results in a small break in the coherency of a relayed image. Gross distortion is defined
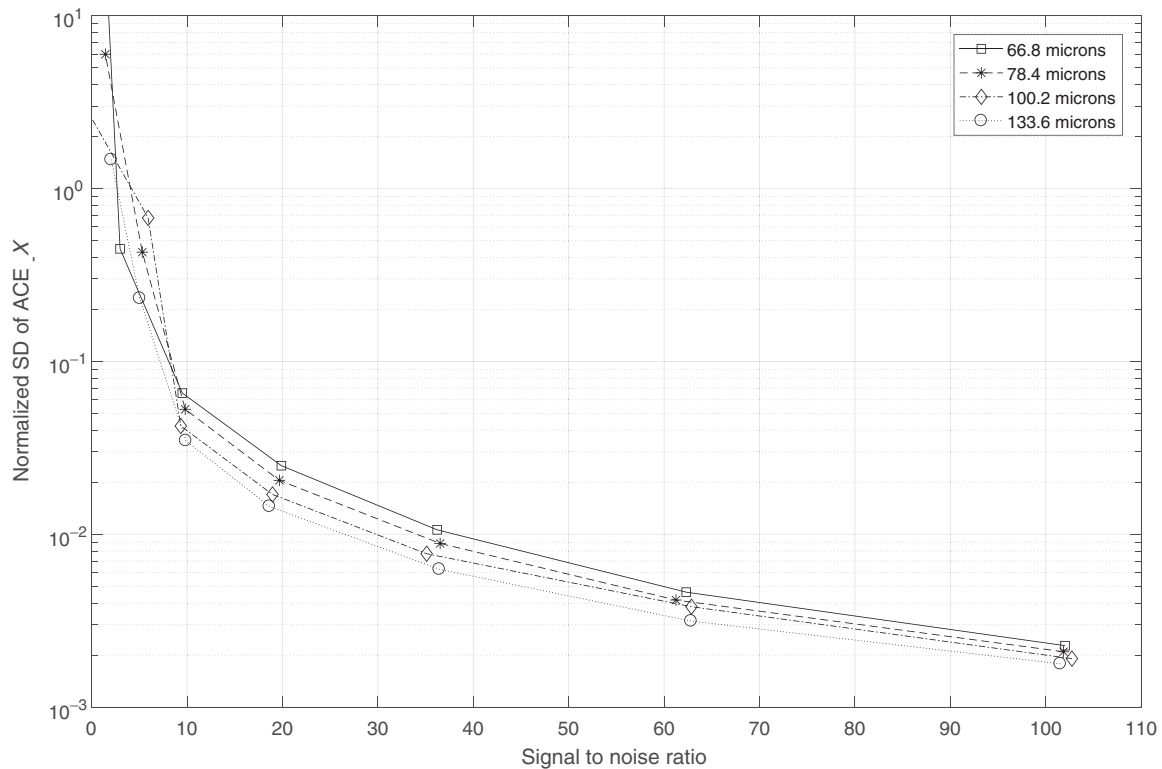
Figure 5. Measured normalised SD of ACE vs. SNR with different spot sizes.

as the distortion that causes a straight line to be imaged as a continuous curve. It is measured as the maximum displacement from a straight line and it ranges from less than 1 to 2% the clear aperture.

Since the spot array in the SHWFS are relayed through the fibre image bundle, the spots' centroiding measurement accuracy would be influenced not only by the factors mentioned earlier as conventional SHWFS, but also exhibits its own unique properties. Various factors like fill factor, fibre image bundle defects, tile angle would make extra contributions to the centroiding measurement accuracy. Hence, these centroid errors cause the reconfigured wavefront to be in error. It is therefore necessary to investigate the impact of those defects on the centroiding measurement accuracy.

4 SIMULATION METHOD

The SHWFS simulation consists of a spatial resolution of 25×25 microlens array (Thorlabs MLA150-7AR) which is available in our laboratory. Its focal length is 6.7 mm with a lens pitch of 150 μm. The simulated telescope aperture is 3.9 m in diameter. The focused image is then sampled by the wound fibre image bundle and re-imaged at the other end with a 1:1 image relay system and captured by the camera.

The accuracy of a reconstructed wavefront is largely dependent upon the determination of spot centre, commonly referred to the 'centroiding' of a focused spot. It is the diffracted

image of the sub-aperture of telescope formed by the lenslet of the microlens array. The standard approach (the first moment calculation) is defined as

$$X_{\mathrm{m}} = \frac{\sum_i^{n_i} \sum_j^{n_j} X_i * I(i, j)}{\sum_i^{n_i} \sum_j^{n_j} I(i, j)}; Y_{\mathrm{m}} = \frac{\sum_i^{n_i} \sum_j^{n_j} Y_i * I(i, j)}{\sum_i^{n_i} \sum_j^{n_j} I(i, j)}, \quad (1)$$

where X_i and Y_j is the coordinate position of the (i, j)th pixel in one sub-aperture of the lenslet. $I(i, j)$ is the input wavefront intensity at the pixel (i, j) on the square sub-aperture having $n_i \times n_j$ pixels. It gives a reasonable pixel accuracy of centroid estimation in real-time calculation with minimal computational time and is widely adopted by adaptive optical community as the most efficient and robust method (Vyas et al. 2009). We use this centroid method throughout the paper.

A Gaussian function defined as

$$I(x, y) = \exp\left(-0.5 * \left(\frac{(X - X_c)^2}{\sigma_x^2} + \frac{(Y - Y_c)^2}{\sigma_y^2}\right)\right), \quad (2)$$

where X_c and Y_c represents the true spot centre and σ_x and σ_y is the standard deviation (SD) of the Gaussian beam in two dimensions. To simplify analysis, these two are assumed the same. Figure 4(a) shows the simulated Gaussian beam on a grid of 1 430 × 1 430 pixels with the beam diameter of 66.8 μm which is close to the airy disk of the focused spot created by each lenslet of the SHWFS available in our lab. Figure 4(b) shows the focused spot sampled by the coherent fibre image bundle with each fibre of 101 pixels in
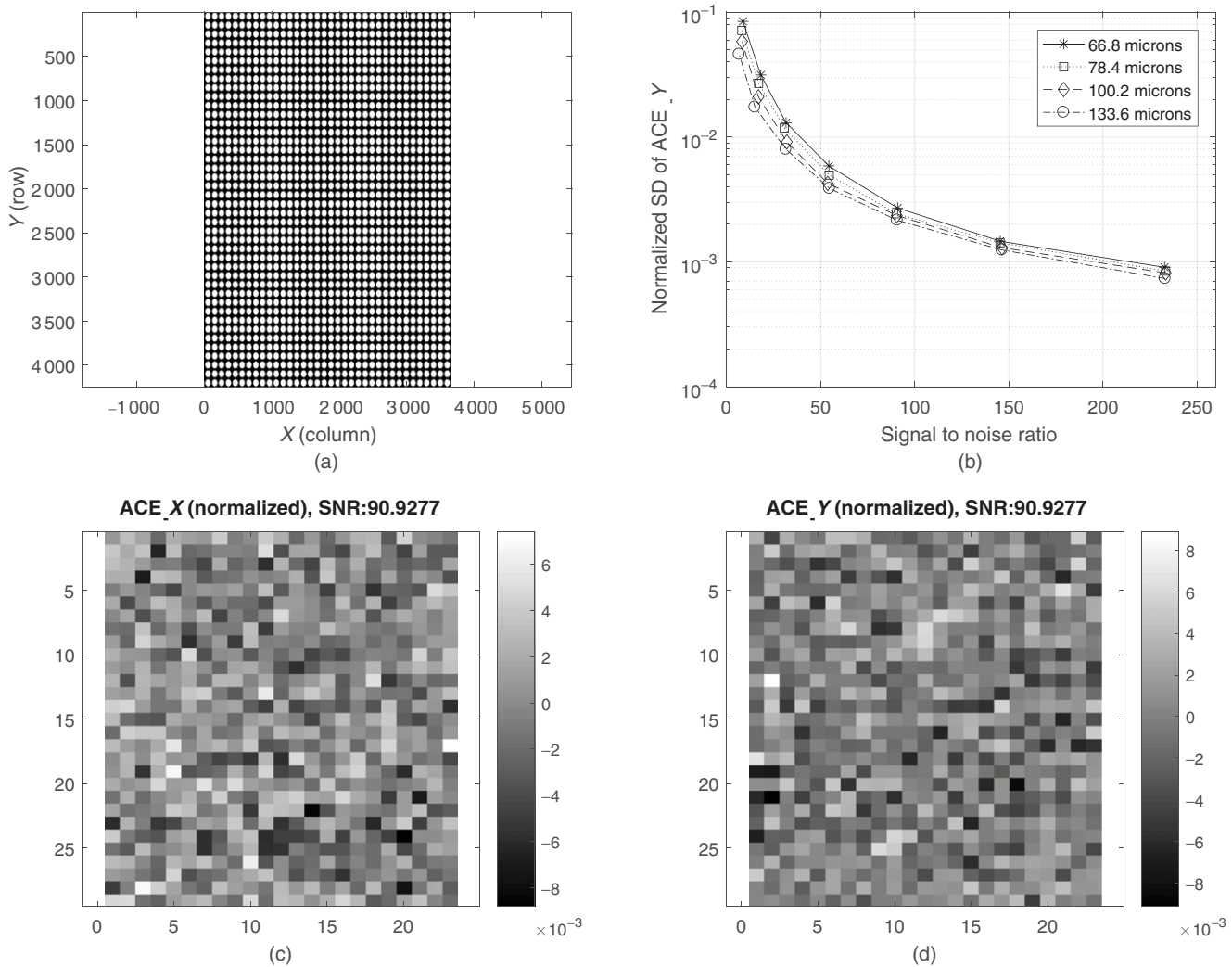
Figure 6. Simulation results. (a) Simulated ideal fibre image bundle without any defects. (b) Normalise measured SD of ACE to the spot size vs. different SNR. (c) Normalised measured ACE_X. (d) Normalised measured ACE_Y when the SNR is 90.

diameter. Figure 4(c) shows the relayed and re-sampled spot on the sCMOS camera. Its typical area of interest (AOI) is about 25×25 pixels on the sCMOS camera with pixel size of 6.5 μm which is Zyla camera available in our lab (Andor 2017). The AOI is determined by the microlens' pitch (the spots spacing). The spot size is chosen to represent the microlens array available for testing in our bench-top laboratory setup. The same methodology can be applied to any configuration of wound fibre bundle SHWFS.

The signal-to-noise ratio (SNR) of the measurement within the AOI can be calculated as

$$\frac{S}{N} = \frac{S * \sqrt{t}}{\sqrt{S + n_{\text{pixel}} * (B + I_d + \frac{R^2}{t})}}, \quad (3)$$

where t is the integration time per exposure, n_{pixel} is the number of pixels in the AOI, S is the signal received within one lenslet, and B is the sky background, I_d and R are dark

current and read noise of the Andor Zyla sCMOS camera, respectively.

To compare the centroiding accuracy at different simulation conditions quantitatively, the absolute centroiding measurement error (ACE) is defined as

$$ACE\_X = X_m - X_c,$$
$$ACE\_Y = Y_m - Y_c,$$
$$ACE\_R = \sqrt{(X_m - X_c)^2 + (Y_m - Y_c)^2},$$

where (X_m, Y_m) is the estimated spot's centre on the detector focal plane, (X_c, Y_c) is the simulated spot's true centre.

The simulation process is as follows:

- Generate a Gaussian beam with a known centre.
- Generate the wound fibre image bundle mask with tile angle randomly chosen between 0 and specified
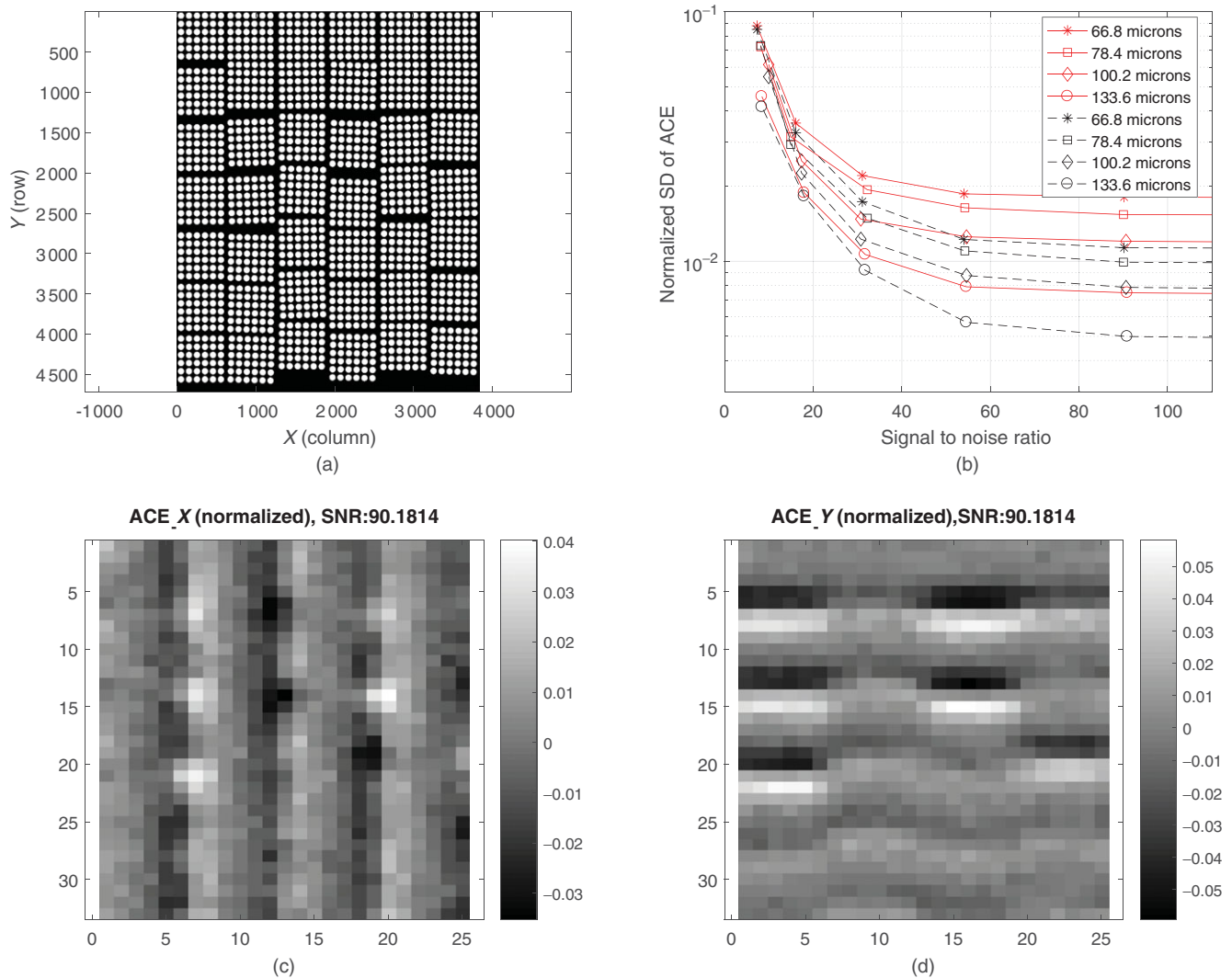
Figure 7. Simulation results. (a) Simulated fibre bundle with tile angle uniform random with range −2 to 2° and chicken wire width uniform random in row is 0 to 2 μm and in column is 0 to 10 μm. (b) Normalised SD of ACE vs. SNR with different spot size. The solid lines are for ACE in row. The dashed lines are for ACE in column. (c) Normalised measured ACE_X. (d) Normalised measured ACE_Y with SNR of 102.

angle with chicken wire row and column width chosen randomly.

- The Gaussian beam is multiplied with the fibre image bundle mask.
- Take the mean intensity of each fibre within the AOI.
- Pixelation (binning) of the image with the detector and add read noise, dark current, and photon noise by using the specification sheet from Andor to the AOI.
- Scan the Gaussian beam along fibre image bundle in two dimensions.
- Calculate the ACE at each position.
- Repeat the same process with a different sizes of the Gaussian beam.

We then normalise the SD of ACE at each simulation condition by the Airy beam size which is 5.81σ, where σ is defined in equation (2).

5 SIMULATION RESULTS

Since the available fibre core size of the wound fibre image bundle is fixed by the manufacturer, we will not simulate the fibre core size impact on the performance of the SHWFS. A fibre diameter of 10 μm with core size of 8 μm is used for all our simulations.

The simulation is done by applying different magnitude of the star received on the wavefront sensor. The measured SNR range from 1 to 100 can be obtained either by increasing the guide star magnitude or the exposure time of the sensor. However, in practice, increasing exposure time is very limited as it would exceed the atmospheric coherence time. For the simulations with SNRs above 80 (for an AOI of 23×23 pixels), it indicates low noise level and SNR lower than 30 represents high noise level or poor sensor imaging. At SNR less than 10, the spot becomes virtually indistinguishable.
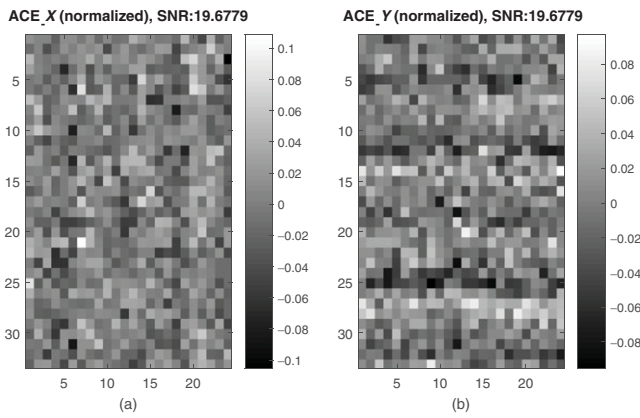
Figure 8. (a) Normalised measured ACE_*X* when SNR is 19. (d) Normalised measured ACE_*Y* when SNR is 19.

Table 1. Shack–Hartmann relative displacements on bundle.

Frame	ΔX (μm)	ΔY (μm)
1	33.2930	15.0079
2	25.2513	11.4464
3	8.4173	3.8198
4	− 18.7698	− 8.7103
5	− 48.1917	− 21.5638

Table 2. Standard deviation of absolute centroid error.[a]

Frame	σ_x (spot)	σ_y (spot)
1	0.0200	0.0193
2	0.0197	0.0165
3	0.0222	0.0184
4	0.0319	0.0244
5	0.0264	0.0290
Mean	0.0240	0.0215

[a]Normalised by dividing centroid by spot diameter.

5.1. Centroiding accuracy baseline of a conventional SHWFS

Figure 5 shows the simulated normalised SD of the ACE vs. SNR when the focused spot size is directly received by sC-MOS camera. The spot size shown in Figure 5 is the equivalent Airy disc size of the Gaussian beam. Note that only ACE for column is shown here as ACE for row is the same. This simulation provides the centroiding accuracy baseline for a conventional SHWFS. Spot size which is in the range from 66.8 to 133.8 µm are studied. The variation of the spot size is to assess the sampling performance of the wound bundle SHWFS. It is shown that the ACE decreases when the SNR is increases for the different sizes of spots. Also, the ACE experiences only small decreases as the spot size gets
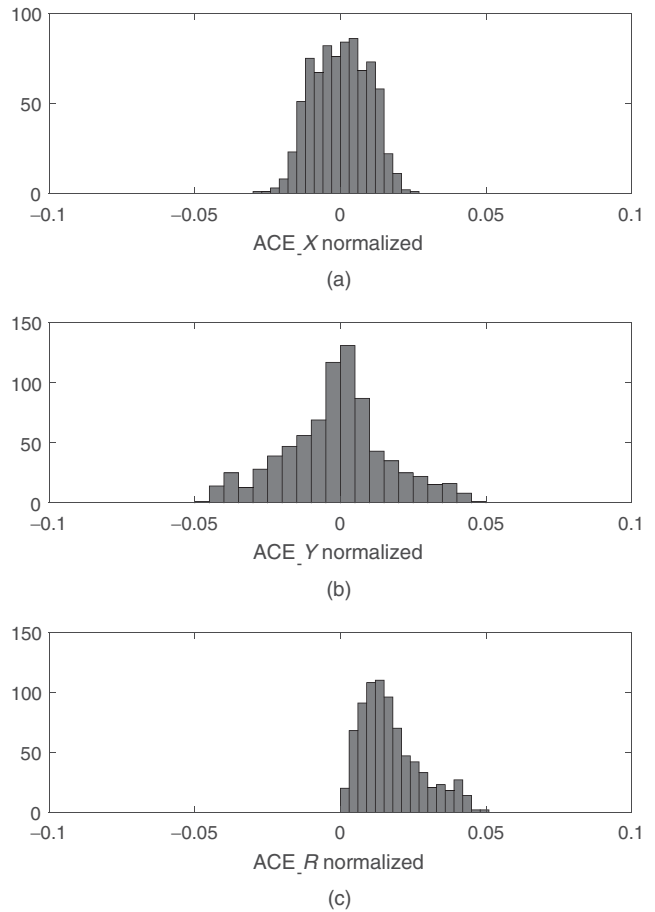
Figure 9. Histogram of ACE for the Figure 7(c), (d) data set in column (top), row (middle), and *R* direction (bottom).

Table 3. Stable probability distribution parameter for absolute centroid error in *x*.[a]

Frame	α	β	γ	δ
1	1.7445	0.3366	0.0101	− 0.0009
2	1.6217	0.6226	0.0090	− 0.0030
3	1.8834	0.2933	0.0117	− 0.0014
4	1.7064	− 0.6796	0.0151	0.0041
5	1.6565	− 0.4803	0.0127	0.0027
Mean	1.7225	0.0185	0.0117	0.0003

[a]Normalised by dividing centroid by spot diameter.

Table 4. Stable probability distribution parameter for absolute centroid error in *y*.[a]

Frame	α	β	γ	δ
1	1.6394	− 0.0549	0.0094	0.0003
2	1.5982	− 0.2850	− 0.2850	0.0082
3	1.6908	− 0.4276	0.0089	0.0020
4	1.7559	0.2048	0.0125	− 0.0003
5	1.5831	0.6168	0.0139	− 0.0042
Mean	1.6535	0.0108	− 0.0481	0.0012

[a]Normalised by dividing centroid by spot diameter.

(a)

(b)

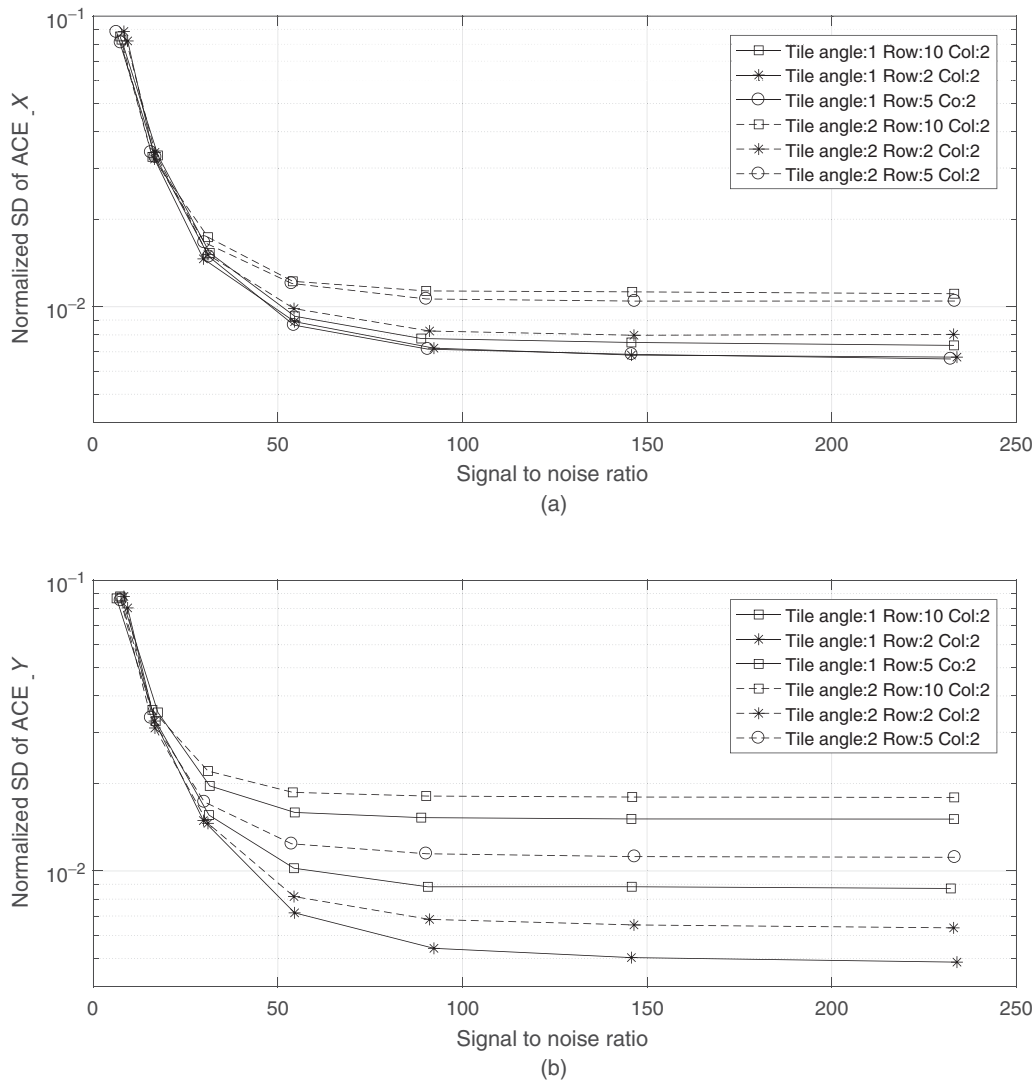**Figure 10.** Measured normalised SD of ACE vs. SNR with spot size of 66.8 μm. (a) in column. (b) in row.

larger. This is expected as under this condition, the measurement error is only related to the camera pixelation error and its read noise. To improve the centroiding accuracy, it is most effective to improve the measurement SNR.

5.2. SHWFS with an ideal fibre image bundle

Figure 6 shows the simulation results when an ideal fibre image bundle is constructed without any defects which is similar to the case for the polymer image fibre bundle. Figure 6(a) shows the image of the simulated fibre image bundle. Figure 6(b) shows the measured centroiding accuracy at row direction vs. SNR with difference spot size. The performance is very similar to the previous simulation where there is no coherent fibre image bundle. Figures 6(c) and (d) show that the normalised ACE when the spot (66.8 μm) scanning through row and column direction, respectively. It

Table 5. Shack–Hartmann reconstructed wavefront.[a,b]

Frame	RMS (μm)
1	0.0182
2	0.0149
3	0.0200
4	0.0210
5	0.0354
Mean	0.0219

[a]Reference wavefront is mean of data sets.
[b]Global tip-tilt terms subtracted from each data set.

is shown that there are no features within the ACE measurements. Note that the peak to valley measurement centroiding error in both directions are very similar. For low SNR < 10, the ACE increases noticeably for smaller spot
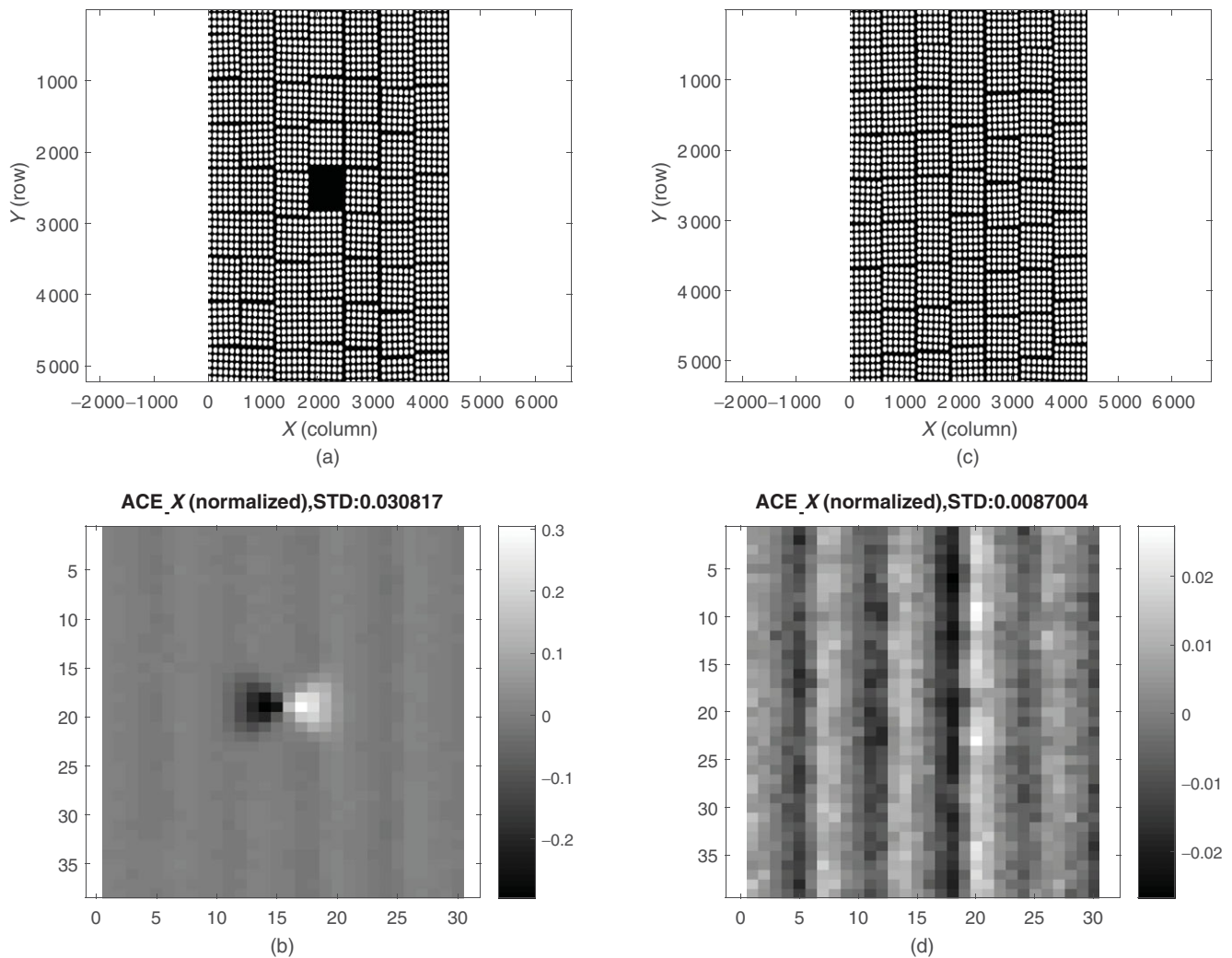
Figure 11. (a) Simulated fibre image bundle with blemish and chicken wire. (b) Simulated fibre image bundle with only chicken wire. (c) Normalised measured ACE_X for simulated bundle(a). (d) Normalised measured ACE_X for simulated bundle (b) with SNR of 90.

sizes. We note the similarity in the ACE between the conventional SHWFS (Figure 5) and that of the ideal fibre image bundle (Figure 6(b)), as the spot is well sampled by the detector.

5.3. Wound fibre image bundle with cell's tile angle and chicken wire defects

Figure 7(a) shows the simulated wound fibre image bundle with the tile angle uniformly random distributed from -2° to 2°. The chicken wire width uniformly random in column is 0 to 2 µm and in row is 0 to 10 µm, respectively. Figure 7(b) shows that the measured normalised SD of ACE vs. SNR with different spot size at both row and column direction. It is shown that the normalised SD of ACE in row is bigger than it in column direction. This is because the chicken wire mean gap in row is five times bigger than the column mean gap. It is also shown that the SD of ACE reduces when
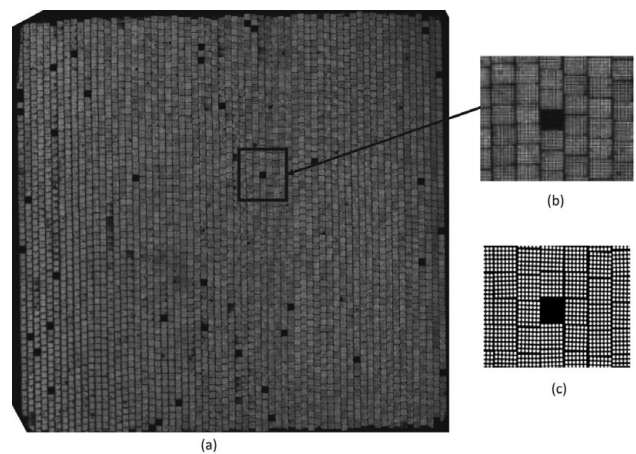

Figure 12. (a) Demo wound bundle used in experimental evaluation. (b) Magnified section of the demo wound bundle. (c) Simulated wound bundle with blemish.
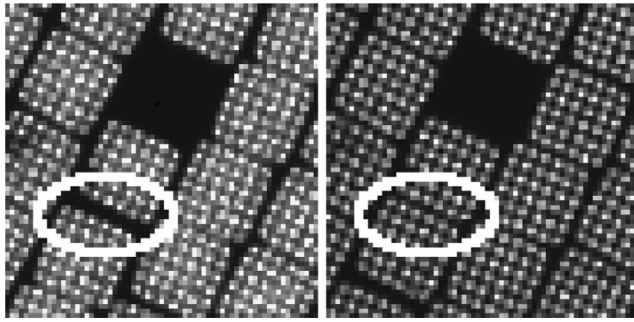
Figure 13. A misaligned tile (relative to surrounding tiles) found by comparing images of the front surface (left) and back surface (right). A non-transmitting tile is also shown at image top.
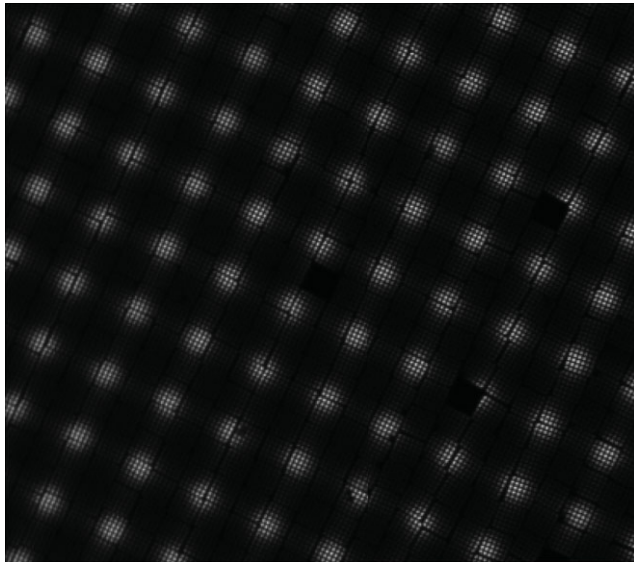

Figure 14. Zoom of Shack–Hartmann spot array as imaged by the demo wound bundle. Each sampled spot shows the resolved fibres and tile structure.

the SNR is increasing. The normalised SD of ACE is also reduced when the spot size increases. This is because that when the spot is small, its focused spot would be sampled by less fibres, hence the line blemishes (chicken wire) impact more on the centroid measurement. However, as the spot size increases, the coverage of fibres average out the bundle's defect effects and hence the measured normalised SD of ACE is less sensitive. Figure 7(c) shows the measured normalised ACE when the spot (66.8 μm) scanning over the column direction. It clearly shows that the measurement error is fluctuated with the chicken wire position in column. Figure 7(d) shows the measured normalised centroid error when the spot (66.8 μm) scanning over the row direction. It is also shown that when the SNR is getting bigger (i.e. SNR > 50), the chicken wire effect becomes obvious. When the SNR is smaller, the chicken wire effects are less important to the ACE since the read noise become the dominant factor.

Figure 8 shows that with SNR of 19 and same fibre image bundle, the measured normalised ACE in both column and row direction. It is obvious that now the centroiding error is not influenced by the chicken wire gap or bundle defects.

Figure 9 shows the histogram derived from Figures 7 (c) and (d) for spot size of 66.8 μm. The SD of the measured ACE, normalised by the spot size, in column is about 0.0115, while in row direction it is about 0.0181.

Figure 10 shows the simulated normalised SD of ACE vs. SNR with different fibre image bundle parameters. It is shown that with the focused spot size of 66.8 μm, the tile angle uniformly random distributed −1 to 1° and −2 to 2° for the fibre wound bundle, respectively. The normalised SD of ACE is decreasing with the SNR increases, however, it is not changing that significantly between these two angle distributions. For the same tile angle distribution, when the chicken wire width changes in row from distribution 0 to 2 μm to the distribution 0 to 10 μm, while the width of column keeps the same distribution 0 to 2 μm, the centroiding accuracy in row direction is noticeably worse. Note that when the SNR over 50, increasing SNR will not improve the centroiding accuracy significantly.

5.4. Comparison of wound fibre image bundle with spot blemish

In the previous section, we simulated the influence of chicken wire width effects to the accuracy of the measured ACE. In this section, we discuss the spot blemish effects on the accuracy of the measured of ACE. Figures 11(a) and (b) show the simulated wound fibre image bundle with and without spot blemish, respectively. The two wound bundles are with similar chicken wire width of 2 μm in both direction and tile angle of 2° simulated the same as previous section. Figures 11(c) and (d) show the measured SD of the ACE corresponding to the two wound bundles. Note that the SNR for both simulation condition is 102. The measured SD of ACE for wound bundle with spot blemish is 0.03, while for bundle without blemish it is 0.009. It is obvious that the measured SD of the ACE increases quite significantly when there is the spot blemish within the wound fibre bundle.

6 EXPERIMENTS

In this section, we present the experimental evaluation of a demo wound fibre bundle from Schott North America. The demo bundle specifications are described in Section 2. The imaging surface is shown in Figure 12. We see that the transmission of the fibres in Figure 12 are relatively uniform and hence suitable for the application of Shack–Hartmann wavefront sensing. We therefore evaluate several aspects of the demo wound bundle: (1) blemishes—non-transmitting tiles; (2) distortion—misaligned tiles; and (3) wavefront measurement.
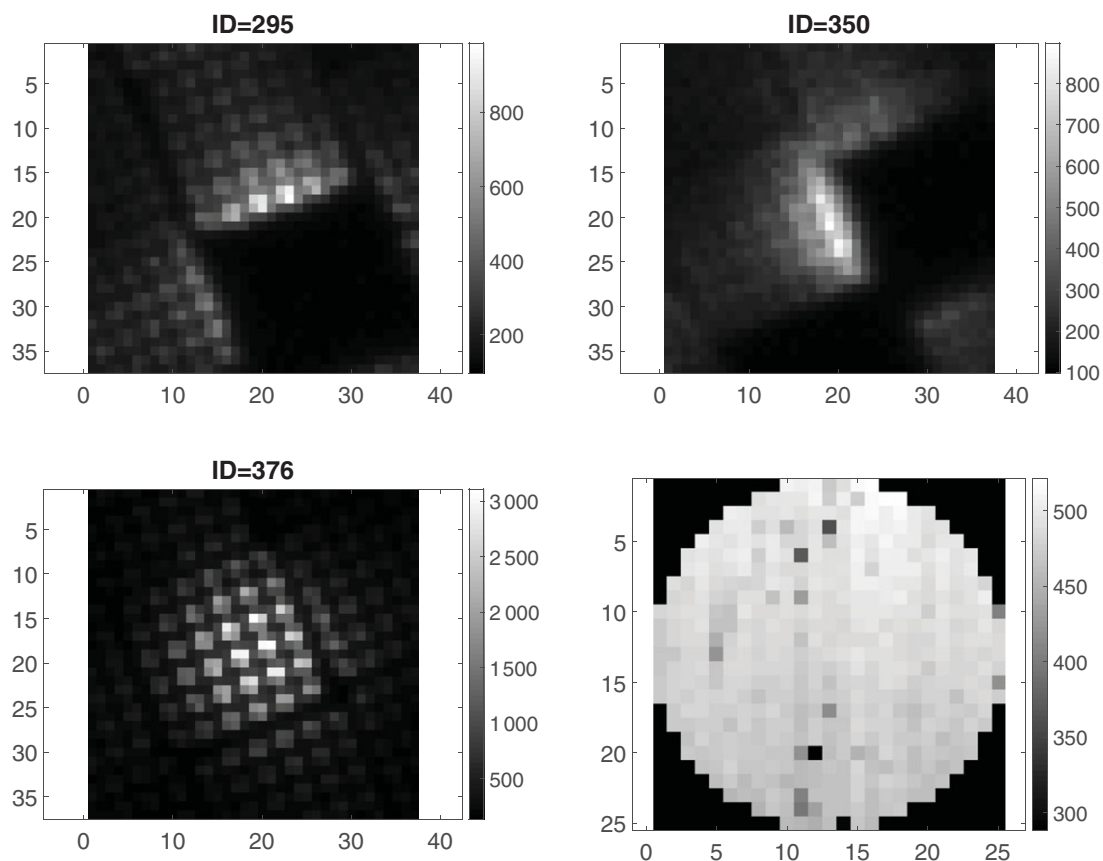
Figure 15. Examples of two poorly sampled spots with low signal counts due to a non-transmitting tile (top); one good sampled spot with high signal counts (bottom-left); Signal-to-noise ratio map for spots of the 25 × 25 Shack–Hartmann array (bottom-right). The spot signal-to-noise ratio is above 300, typical around 500 for a box size 37 × 37 pixels. Data taken from Frame#1.

6.1. Blemishes—non-transmitting tiles

The demo wound fibre bundle has a number of non-transmitting tiles (blemishes) observed as dark squares in Figure 12 and zoom shown in Figure 13. We measured about 35 full and 12 partial non-transmitting tiles. The total non-transmitting tiles equate to about 1% of the imaging surface area. The Schott commercial wound bundle specifications for a comparable size, state a much lower defect count, less than six non-transmitting tiles. Non-transmitting tiles could potentially be avoided during the alignment of the microlens array to the bundle imaging surface. The spots that do coincide with a non-transmitting tile (few in number) can be excluded from the wavefront reconstruction. Alternatively, the implementation of calibration algorithms for those spots might suffice.

6.2. Distortion—misaligned tiles

We define misaligned tiles (distortion) as tiles that are displaced relative to surrounding tiles found by comparing the front and back surfaces of the wound bundle. An example of a misaligned tile is shown in Figure 13. A misaligned tile can be displaced as much as a fibre core (10 μm) and can result in an error the Shack–Hartmann spot location. The misaligned tiles can also occur between columns where the entire column can have a slight vertical height offset. Individual misaligned tiles, an example in Figure 13 are less in number (only few observed) than the non-transmitting tiles. A misaligned tile is less of an issue as the SHWFS can be nulled to the reference wavefront. The SHWFS is primarily concerned with the spot displacement from its reference position.

6.3. Wavefront measurement

To examine how the non-transmitting and misaligned tiles impact a wound bundle-based SHWFS, we investigate the wavefront measurement residuals for different displacements of the spot array. The unique sampling of the spot array and the resulting wavefront measurement can be compared. The difference between the tip-tilt subtracted wavefronts can then be attributed to the bundle sampling effects of the non-transmitting and misaligned tiles. An example image of the Shack–Hartmann spot array is shown in Figure 14.
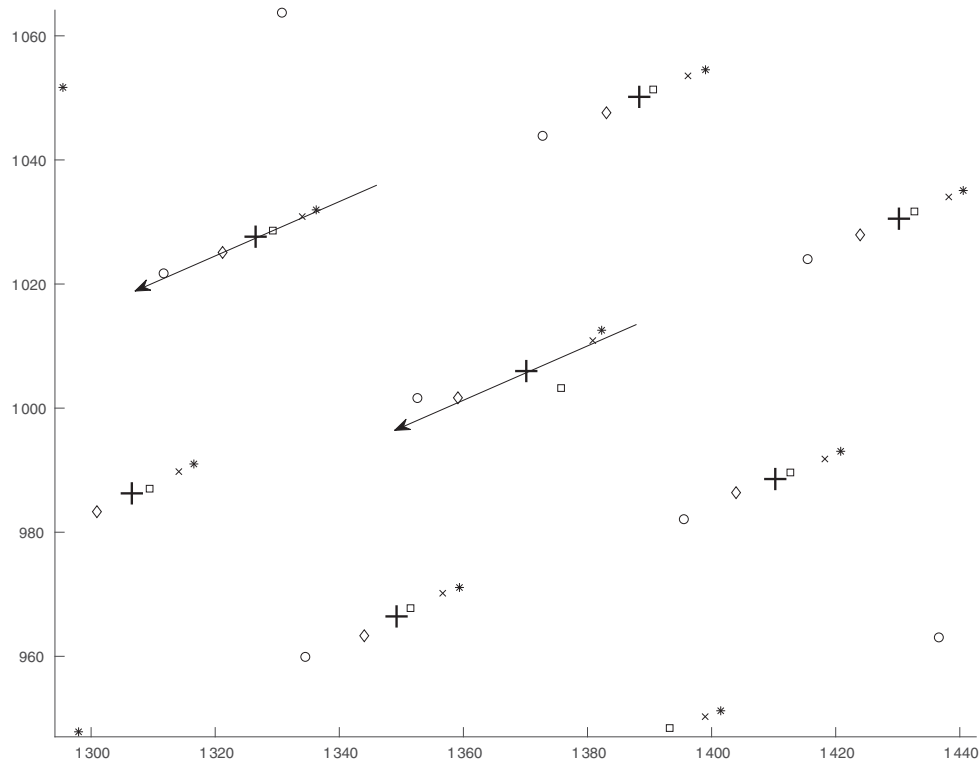
Figure 16. Subset of centroid positions for five frames of Shack–Hartmann data. Each frame having a fraction of a spot displacement (approx. North-East to South-West direction). The displacement vector overlays for a good sampled spot (left) and a poor sampled spot (centre). The plus (+), symbols denote the average centroid or reference frame. The coordinates are in raw pixels.

The Shack–Hartmann array is formed by using a microlens array (Thorlabs MLA150-7AR) having a lens pitch of 150 μm and focal length of 6.7 mm, focused onto the front surface of the wound fibre bundle. The bundle back surface is re-imaged onto an Andor Zyla 5.5 camera with a pixel size 6.5 μm using a 2x telecentric lens (Edmund Optics #58-431). The spot centroid calculated using the first moment calculation as described in Section 4. The spot diameters formed by the microlens array are approx. 71 μm given by 2.44 λN, where λ is wavelength of 632 nm and N is the f-number ($f/\#$).

Examples of spot sampling and the SNR for Frame#1 are shown in Figure 15. We note from Figure 15 that the SNR is relatively high, typically about 500, so the expected centroid error due to noise factors of the order $\sigma = 0.002$ spot diameters. Therefore, from the simulations, we expect the bundle sampling errors to dominate the centroid errors. From Figure 15, we see that the poorly sampled spots are both impeded by a non-transmitting tile that results in a centroid measurement error due to irregular spot shape changes as well as a lower SNR.

To compare with simulations, the equivalent Gaussian spot fitted to the microlens theoretical airy disk has a SD of $\sigma \approx 0.42 \lambda N$, or $\sigma = 12.2$ μm. The equivalent spot diameter is approx. 5.81σ and encircles 99.6% of the energy of the

Gaussian spot. The diameter of the spot on the detector is approx. 22 pixels because of the 2x magnification re-imaging lens. The analysis consists of five frames each having a unique microlens array displacement as listed in Table 1. The range in displacement of the spot array pattern being approximately a spot diameter, as shown in Figure 16. This was achieved by moving the microlens array in the lateral position using a positioning stage. This allows for the sufficient dithering of the bundle surface in order to quantify the performance in centroid measurement.

An example of spot centroid measurement errors are shown in Figure 16. From Figure 16, we see that the centroid of the poorly sampled spot for each of the five frames deviates from its linear displacement vector unlike its neighbouring sampled spots. This is due a non-transmitting tile that erroneously biases the spot centroid measurement. The smaller deviations of the neighbouring sampled spots in Figure 16 are due to structure and layout of the wound bundle.

To see how these sampling issues affect the Shack–Hartmann array, consider the ACE with example shown in Figure 17. The ACE is calculated by first subtracting the reference (local spot averages from all frame data) from each individual data set. It is assumed that reference frame averages out the sampling errors. Next, the global tip-tilt displacement is subtracted by calculating and subtracting the
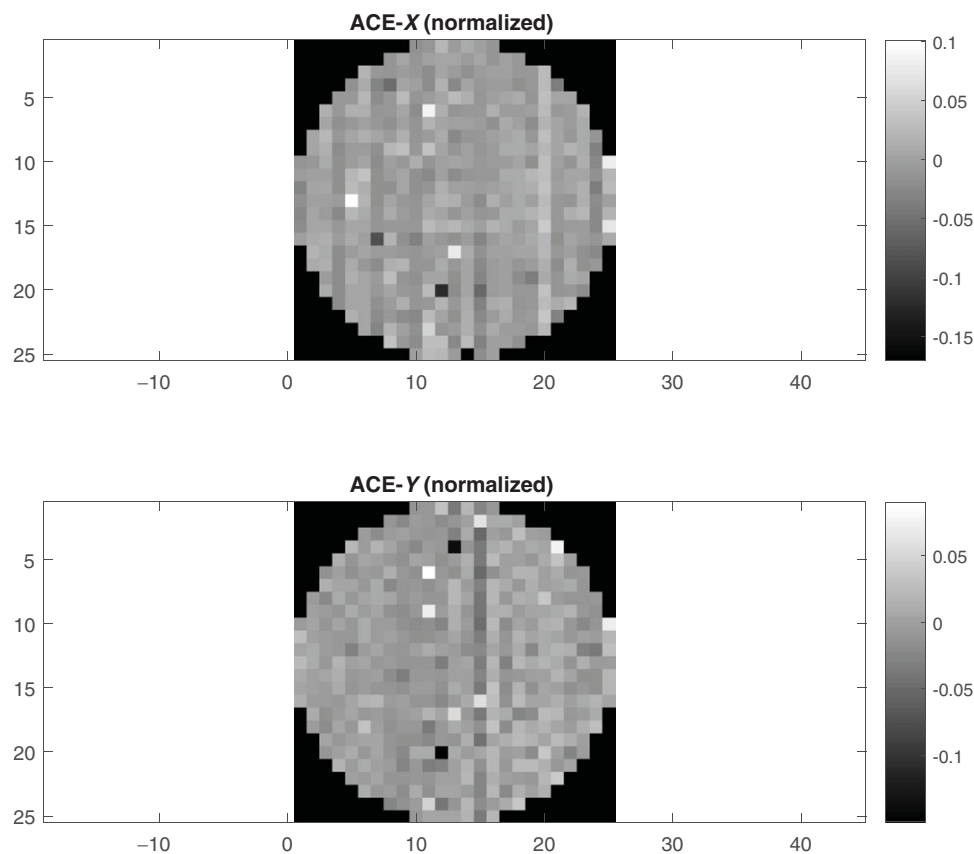
Figure 17. Absolute Centroid Error (ACE) for Frame#1 in X direction (top) and Y-direction (bottom). Error is normalised by the spot diameter. The X, Y axis units are in lenslet spacings.

mean displacement of all spots in the array. The residual displacement of individual spot are then normalised by the theoretical spot diameter. The normalisation being a useful comparison tool for other systems. A histogram of the ACE computed from Figure 17 are shown in Figure 18. The ACE SD for X and Y (σ_x and σ_y) are listed in Table 2. We get a mean $\sigma_x = 0.0240$ and $\sigma_y = 0.0215$ that can be compared to the simulation results shown in Figure 7–11. From Table 2, we note a similarity in the values for the ACE SD, with Y being slightly less than X, except for Frame#5. A reason for the lower Y values could be the relative alignment of the displacement vector to the wound bundle row/col structure.

The parameters for a stable distribution fit to the ACE for X and Y data are listed in Tables 3 and 4. A stable distribution is used as it is suitable for modelling heavy tails and skewness. A stable distribution is helpful in generating errors for fast simulations that model the wound bundle for wavefront sensing applications. The first parameter α, is the shape parameter describing the tails. The second parameter β, is the shape parameter describing the skewness. The third and fourth parameters, γ and δ are used for the scale and location. From Tables 3 and 4, we note the similarity of α for X and Y being 1.7225 and 1.6535. This gives a distribution with a

larger tail (narrower peak) compared to Gaussian distribution which has $\alpha = 2$.

The wavefront is reconstructed from the Shack–Hartmann centroid data using the modal method using Zernike polynomials. The dimension of the Shack–Hartmann array being a circular pupil with 25 lenslets across the diameter. The number of Zernike modes being limited to 60 modes. The reference for the Shack–Hartmann array being the average of the corresponding local centroid over all frames, as shown in Figure 16.

For each frame, the reference centroid data was subtracted and then the wavefront reconstructed. The piston, tip-tilt Zernike terms set to zero (Z1 = 0, Z2 = 0, Z3 = 0), and then the RMS of the wavefront computed. Removing the wavefront tip-tilt component compensates for the displacement of the Shack–Hartmann array allowing the sampling effects to dominate the measured wavefront. The results for the Frame#1 is shown in Figures 19 and 20. The summary wavefront RMS results can be found in Table 5. The mean RMS of the tip-tilt subtracted wavefront from Table 5 is $\sigma = 0.0219$ μm or $\sigma \approx \lambda/30$. We note that the mean RMS is skewed by Frame#5 having $\sigma = 0.0354$ μm. For a classical Shack–Hartmann array with a CCD, we expect the RMS of the tip-tilt subtracted wavefront
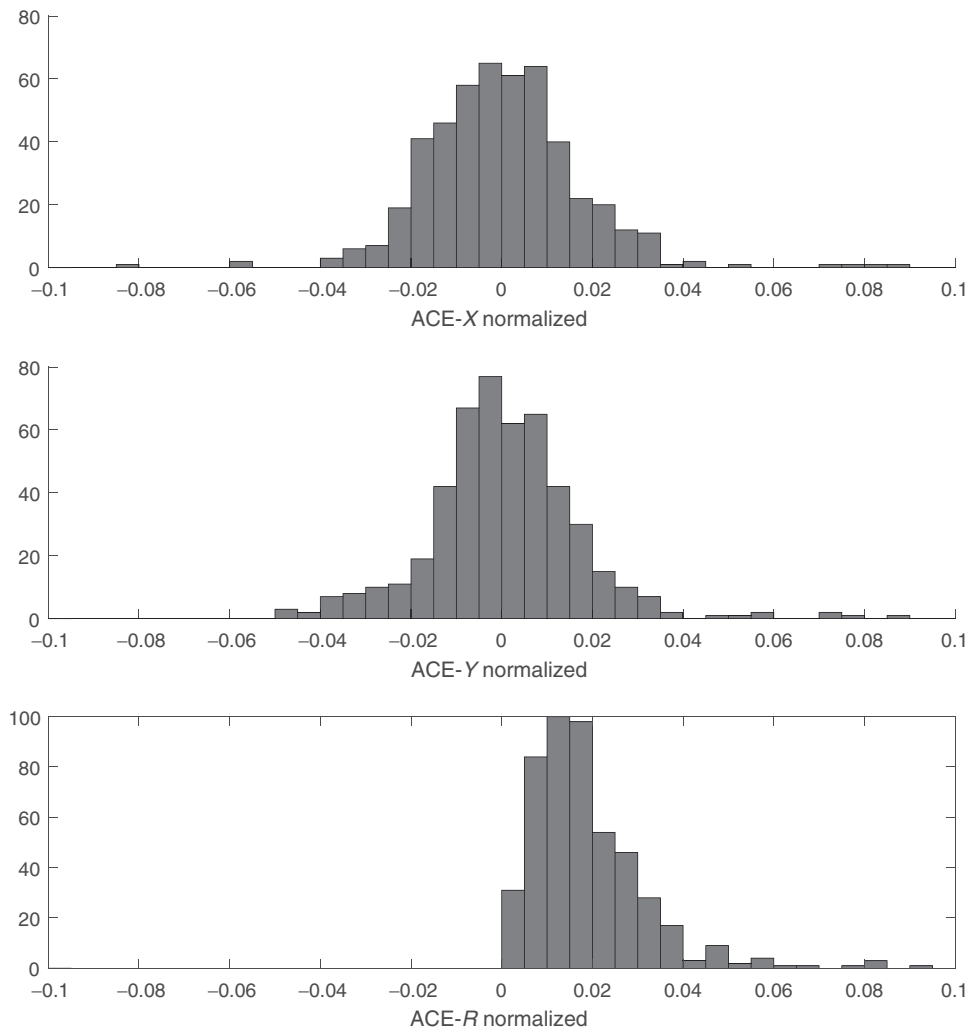
Figure 18. Histogram of Absolute Centroid Error (ACE) for Frame#1 in *X* direction (top), *Y*-direction (middle), and $R = \sqrt{X^2 + Y^2}$ (bottom). Error is normalised by the spot diameter.

for different displacements to be near zero (i.e. no sampling effects).

7 CONCLUSIONS

In this paper, we have investigated the feasibility of using a wound fibre image bundle to relay the image formed by a SHWFS. The key advantage being that the wound bundle facilitates a compact wavefront sensor design that can fit into a Starbug built for the upcoming extremely large telescopes. The application of the technology allows the efficient positioning of many wavefront sensors over the focal plane for MOAO. We are particularly interested in seeing how this technology can benefit the GMT.

We have provided a description of the experimental setup and the limitations expected from the wound fibre image bundle technology, such as the 'chicken wire' and spot blemishes (non-transmitting fibres). We have characterised the perfor-

mance of a demo wound bundle, provided by Schott North America.

The throughput of the demo wound fibre image bundle measured from 40 to 50% over 400 to 1 600 nm. This is expected decrease slightly with increased length but provides the flexibility for cable management (i.e. 4-m lengths should be practical). The transmission in the near-infrared and improved performance of low-noise high-read out detectors allows the prospect for near-infrared wavefront sensing (i.e. wavelengths around 1 600 nm should be practical).

Simulations have been performed to understand the performances of the demo wound fibre for wavefront sensing. The simulations clearly show that for a low SNR (i.e. less than 30) the wound fibre imaging bundle is not the limiting factor. It is only at high SNRs that the 'chicken wire' limitation is apparent and sets the overall centroid error noise floor. It is also shown that the spot blemish plays an
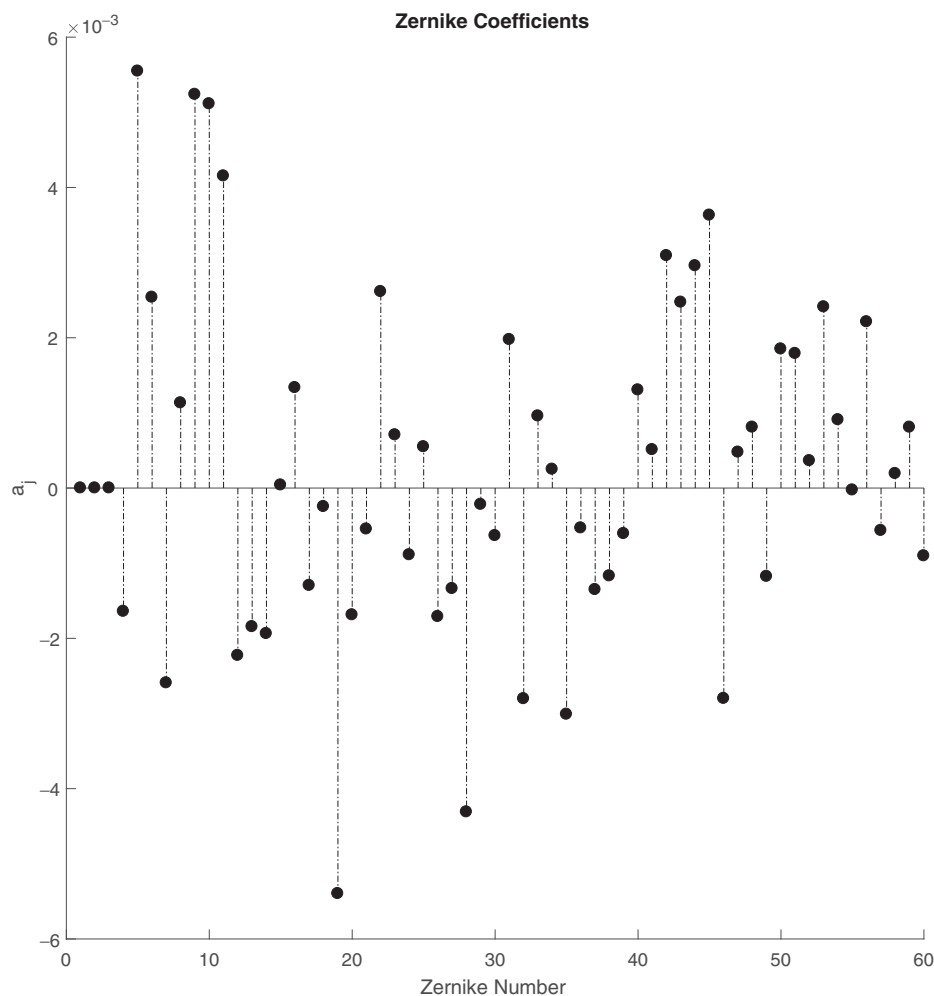
Figure 19. Zernike coefficients for Frame#1. The tip-tilt coefficients being set to zero.

important role for the centroiding measurement accuracy. It can increase the SD of ACE significantly. It is necessary to define the tolerance of the spot blemish within the wound bundle. Our simulation shows that the tolerance less than 1% will be needed. While the tolerance for chicken wire width is less tight.

Experiments performed on the demo wound fibre image bundle examined the (i) non-transmitting tiles (spot blemishes); (ii) misaligned tiles (distortion); and the (ii) wavefront measurement. This allows us to examine that which are not easily modelled through simulations. We measured approx. 35 full and 12 partial non-transmitting tiles, which total less than 1% of the imaging surface. Misaligned tiles between front and back imaging surfaces are much fewer in number, the largest of misalignment being around 10 microns. Keeping in mind that the commercial bundle has much better specifications (less than six blemishes for an equivalent sized bundle).

We measured the normalised centroid error of the demo wound fibre image bundle to have a mean SD, $\sigma_x =$ 0.0240, and $\sigma_y = 0.0215$ of the spot diameter. These values are similar to the simulation for the Y component. We have reported the parameters for stable distribution fits to the normalised centroid errors. The stable distributions can be used to model the centroid errors to speed up simulations.

The mean RMS of the resulting wavefront is measured to be $\sigma = 0.0219\,\mu$m or equivalently $\sigma \approx \lambda/30$. Subject to further investigation, it may be possible with calibration to further reduce the wavefront error induced by the wound bundle. However, this level of error should be acceptable for most wavefront sensing applications.

We therefore conclude that the use of a wound fibre imaging bundle is feasible for Shack–Hartmann wavefront sensing. Further, incorporating the wavefront sensor into a Starbug for focal plane positioning provides enhanced science opportunities for future astronomical instrumentation. We are now planning the development of a Starbug wavefront sensor suitable for large telescopes.
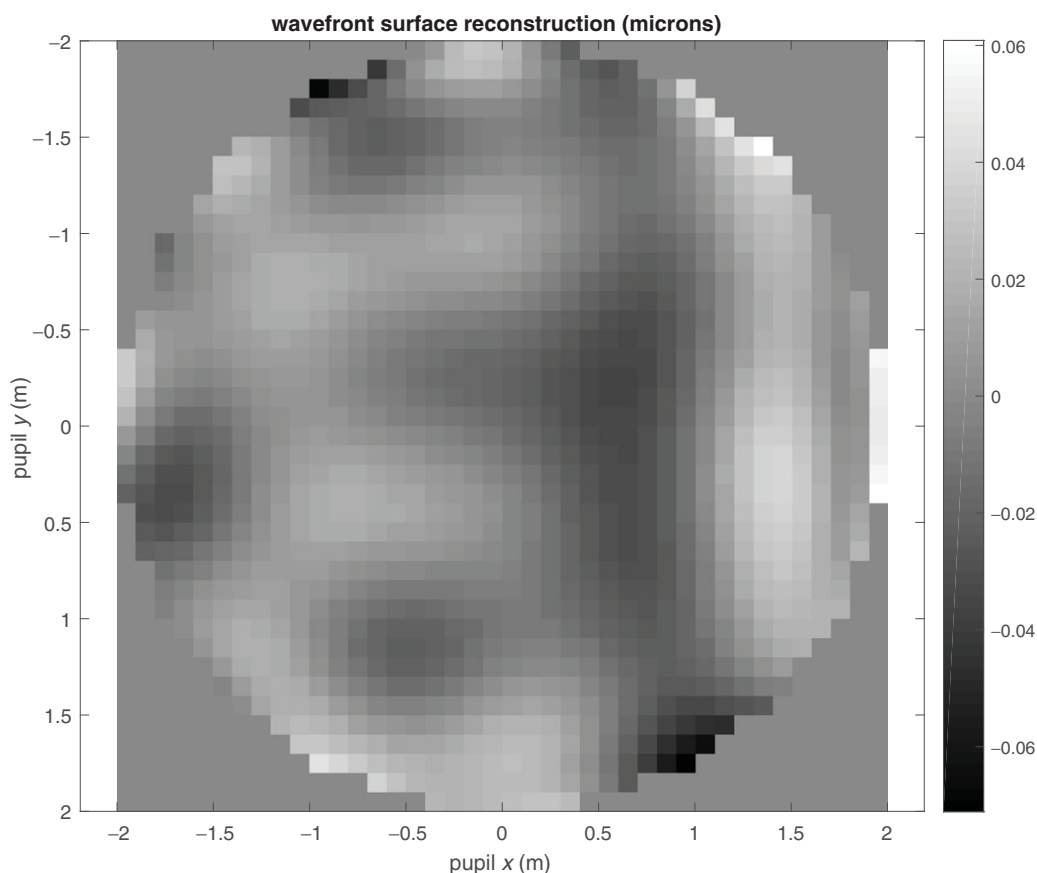
wavefront surface reconstruction (microns)

Figure 20. Wavefront (tip-tilt subtracted) for Frame#1. The RMS is 0.0182 microns.

References

Ammons, S. M., Johnson, L., Laag, E. A., Kupke, R., Gavel, D. T., Bauman, B. J., & Max, C. E. 2010, PASP, 122, 573

Andor, O. C., 2017, Zyla sCMOS Camera: Speed and Sensitivity for Physical Science Imaging and Spectroscopy

Gilbert, J., et al. 2012, in Proc. SPIE, Vol. 8450, Modern Technologies in Space- and Ground-based Telescopes and Instrumentation II, 84501A

Goodwin, M., Richards, S., Zheng, J., Lawrence, J., Leon-Saval, S., Argyros, A., & Alcalde, B. 2014, Proc. SPIE, 9151, 91514T

Goodwin, M., Zheng, J., Lawrence, J., Richards, S., & Leon-Sava, S. 2015, in Adaptive Optics for Extremely Large Telescopes 4 – Conference Proceedings, 12

Hardy, J. 1998, Adaptive Optics for Astronomical Telescopes (New York: Oxford University Press)

Irwan, R., & Lane, R. G. 1999, Appl. Opt., 38, 6737

Nightingale, A. M., & Gordeyev, S. 2013, OptEn, 52, 071413

Ono, Y. H., et al. 2016, in Proc. SPIE, Society of Photo-Optical Instrumentation Engineers, 990910

Richards, S. N., et al. 2017, PASA, 34, 8

SCHOTT, North America. 2007, An Introduction to Fiber Optic Imaging (2nd edn.; Southbridge: SCHOTT North America)

Staszak, N. F., et al. 2016, in Advances in Optical and Mechanical Technologies for Telescopes and Instrumentation II, 99121W

Thomas, S., Fusco, T., Tokovinin, A., Nicolle, M., Michau, V., & Rousset, G. 2006, MNRAS, 371, 323

Vyas, A., Roopashree, M., & Prasad, B. 2009, arXiv:0908.4328

Zheng, J., Richards, S., Goodwin, M., Lawrence, J., Leon-Saval, S., & Argyros, A. 2014, in Adaptive Optics Systems IV, 91482E